SCIENCE CHINA
Information Sciences

• RESEARCH PAPER •

January 2026, Vol. 69, Iss. 1, 112404:1–112404:12
https://doi.org/10.1007/s11432-025-4599-8

Heat-sensitive mode-localized current sensor with ultra-high sensitivity

Han LI, Yongcun HAO* & Honglong CHANG

Ministry of Education Key Laboratory of Micro and Nano Systems for Aerospace, School of Mechanical Engineering, Northwestern Polytechnical University, Xi'an 710072, China

Received 3 April 2025/Revised 17 June 2025/Accepted 16 September 2025/Published online 4 January 2026

Abstract Mode-localized sensors are a class of ultra-sensitive resonant sensors that leverage the mode localization effect of weakly coupled systems for signal detection. In this study, a high sensitivity MEMS current sensor based on mode localization is proposed, utilizing a heat-sensitive structure to enhance sensitivity. The heat-sensitive V-shaped beam generates thermal expansion forces in response to current-induced Joule heating, altering the stiffness of weakly coupled resonators and leading to a change in amplitude ratio. The current sensor based on the mode localization principle achieves the highest current resolution in the field of MEMS current sensors. Compared to previous mode-localized current sensors employing shunt resistors, the proposed design achieves a 10-times improvement in amplitude ratio sensitivity. Through rigorous experiments, the sensor demonstrates a noise floor of 2.7 nA/$\sqrt{\text{Hz}}$ and a resolution of 5.9 nA, achieving a 30-times enhancement over previous designs. The proposed sensor achieves the highest resolution among reported microelectromechanical system current sensors and outperforms handheld digital multimeters, laying a strong foundation for the development of next-generation miniaturized, high-precision current sensing technologies.

Keywords mode-localized, current sensor, V-shaped beam, thermal expansion force, ultra-high sensitivity

Citation Li H, Hao Y C, Chang H L. Heat-sensitive mode-localized current sensor with ultra-high sensitivity. Sci China Inf Sci, 2026, 69(1): 112404, https://doi.org/10.1007/s11432-025-4599-8

1 Introduction

Accurate current measurement is essential for power management [1], biomedical monitoring [2], and particle detection [3], driving the need for high-sensitivity sensors. Digital multimeters (DMMs) are widely used for electrical measurements, with benchtop models offering high resolution but being bulky and unsuitable for portable applications. In contrast, handheld DMMs are compact and convenient but suffer from significantly lower resolution, which severely limits their applicability in precision measurements. Therefore, there is a growing need to develop miniaturized current sensing devices that can achieve both high resolution and compact size to meet the demands of modern applications.

In recent years, various novel current sensing strategies have been explored to address the limitations of conventional approaches. A wide range of current sensors has been developed based on magnetic effects, such as Hall effect [4], Rogowski coil [5], magnetic metal film [6], fluxgate [7], and giant magnetoresistance [8]. However, these approaches are susceptible to external magnetic field interference and limited sensitivity, constraining their applicability in precision measurements. To address these challenges, various innovative methods and principles have been reported. For instance, high-sensitivity giant magnetoimpedance sensors based on novel CoFeNiSiB amorphous ribbon meanders enable current sensing at ampere-level ranges [9]; a diamond-based quantum sensor has demonstrated high-precision current sensing capabilities up to 400 A [10]; fiber-optic sensors utilizing polarization-bias-added structures have enabled high-current AC measurements [11]; a DC current sensor based on the surface acoustic wave principle achieves a detection limit of 0.05 mA [12]; and conducting polymer composites such as polyaniline/methylcellulose have been investigated for stable, low-current sensing in supercapacitor applications, achieving detection limits down to 0.05 mA [13]. Despite these advances, challenges remain in simultaneously achieving miniaturization and higher resolution in current sensing devices.

The advancement of microelectromechanical system (MEMS) technology has enabled the development of high-performance sensors with possibility [14–17]. Especially mode-localized sensors, leveraging the amplitude ratio (AR)

* Corresponding author (email: haoyongcun@nwpu.edu.cn)

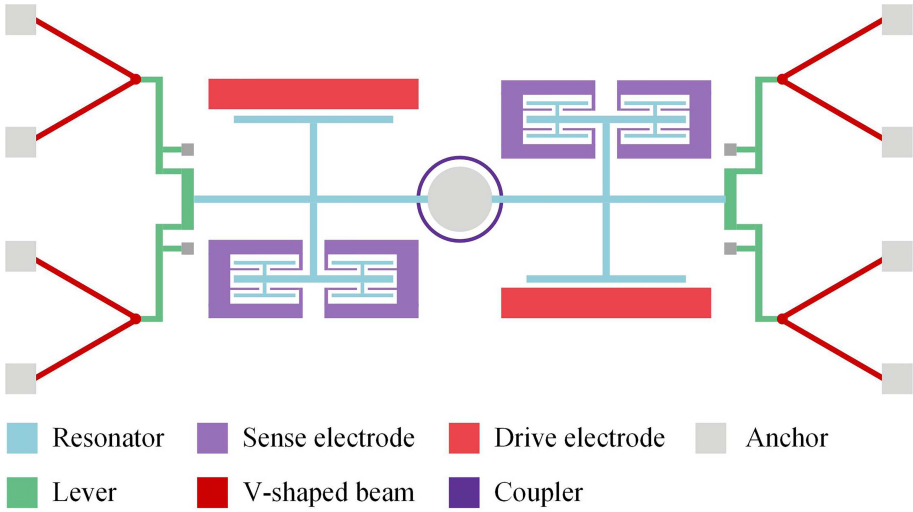

Figure 1 (Color online) Schematic diagram of the mode-localized current sensor.

as the output dimension of weakly coupled resonator systems (WCRs), have emerged as a promising approach. The mode localization phenomenon occurs when a weak stiffness perturbation disrupts the balance of WCRs, leading to an energy redistribution. This effect has been successfully applied in mass [18], acceleration [19, 20], magnetic [21], electrostatic charge [22], and voltage detection [23], demonstrating its potential for ultra-high sensitivity applications [24].

In our previous work, we successfully designed the first mode-localized current sensor, where the current was converted into voltage via a shunt resistor and then detected [25]. In this study, a novel MEMS current sensor is proposed, utilizing a thermally induced stiffness perturbation in a weakly coupled resonator system. The input current flowing through a V-shaped beam generates localized Joule heating, inducing thermal expansion that alters the stiffness of the resonator structure. This results in a measurable change in AR, enabling highly sensitive current detection.

Compared with conventional current sensors, the proposed mode-localized current sensor offers an ultra-high sensitivity. In this study, we experimentally validate the sensor's performance by evaluating its sensitivity, noise floor, and resolution. The results demonstrate that mode localization provides a viable and highly sensitive approach for current sensing, paving the way for the integration of MEMS current sensors with high resolution and miniaturization potential.

2 Device design and theory analysis

2.1 Device design of the current sensor

The mode-localized current sensor, as illustrated in Figure 1, includes WCRs, sense electrode, drive electrode, lever, V-shaped beam, and anchors. The WCRs consist of two resonators connected by a ring-shaped coupler. Since the coupling stiffness is significantly lower than that of the resonators, a weak coupling effect is established. The resonators are symmetrically placed and oscillate only in the vertical direction of the resonator. The drive electrode applies an AC voltage signal to the resonator, inducing vibrations. These vibrations generate an AC, which is measured by the sense electrode to determine the resonator's displacement. The V-shaped beam is the key structure of the current sensor. It receives the external current signal and converts it into thermal expansion force through thermal deformation, which is amplified by a lever and applied to the resonators.

The working principle of the current sensor is as follows. First, the external current is input through the V-shaped beam, generating Joule heat. The beam expands due to thermal deformation, producing thermal expansion force. Two symmetrically placed V-shaped beams on each resonator cancel out any off-axis thermal expansion forces. The thermal expansion force is then amplified by a lever and applied axially to the resonators, inducing the mode-localization effect in the WCRs. The current redistributes energy in the WCRs, leading to changes in the resonators' amplitudes. The current value is determined by measuring the amplitude ratio between the two resonators. Table 1 shows the dimension parameters of the structure.

Table 1 Parameters of the current sensor.

Parameters	Value
Beam length of resonators	600 μm
Beam width of resonators	6 μm
Inner radius of the coupler	310 μm
External radius of the coupler	316 μm
Gap between drive comb	2.5 μm
Overlap length of drive comb	11 μm
Gap between sense capacitor	2.5 μm
Length of sense capacitor	110 μm
Length of V-shaped beam	2000 μm
Width of V-shaped beam	20 μm
Angle of V-shaped beam	60°

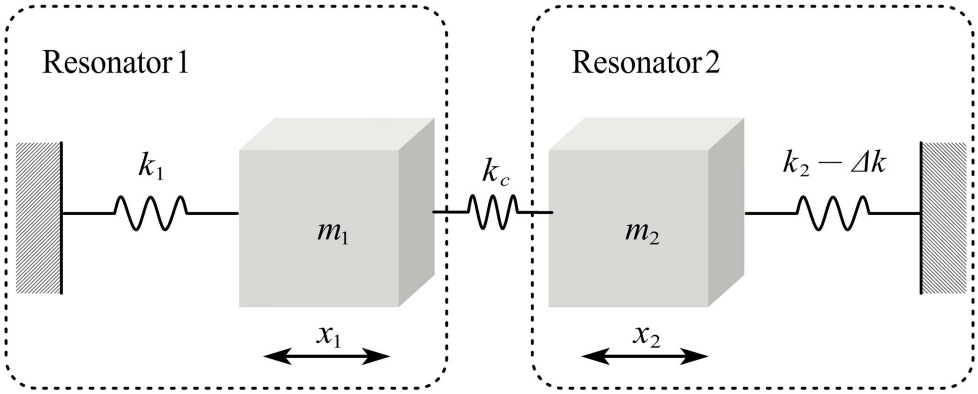

Figure 2 Mass-spring model of the WCRs.

2.2 Theory analysis of the weakly coupled resonators

The WCRs can be simplified to a mass-spring model in ideal conditions without damping, as shown in Figure 2. Theoretically, the WCRs are symmetric, with identical masses and stiffness for both resonators ($k_1 = k_2 = k$, $m_1 = m_2 = m$). The two resonators are weakly coupled by a mechanical coupler, whose stiffness k_c is much smaller than that of the resonators ($k_c \ll k$). The stiffness perturbation Δk caused by the current is also much smaller than k ($\Delta k \ll k$). The dynamic equation of the current sensor is given in

$$\begin{cases} m\ddot{x}_1 + (k + k_c)x_1 - k_c x_2 = 0, \\ m\ddot{x}_2 + (k + k_c - \Delta k)x_2 - k_c x_1 = 0, \end{cases} \tag{1}$$

where x_1 and x_2 are the vibration displacements of the two resonators.

The resonant frequencies and amplitude ratios of the first two vibration modes are given by [26]

$$\begin{cases} \omega_1 = \dfrac{2k - \Delta k + 2k_c - \sqrt{\Delta k^2 + 4k_c^2}}{2m}, \\ \omega_2 = \dfrac{2k - \Delta k + 2k_c + \sqrt{\Delta k^2 + 4k_c^2}}{2m}, \end{cases} \tag{2}$$

$$\begin{cases} \mathrm{AR}_1 = \dfrac{\Delta k + \sqrt{\Delta k^2 + 4k_c^2}}{2k_c}, \\ \mathrm{AR}_2 = \dfrac{\Delta k - \sqrt{\Delta k^2 + 4k_c^2}}{2k_c}. \end{cases} \tag{3}$$

The sensitivity based on the amplitude ratio of the WCRs is expressed as follows:

$$S_k = \left| \frac{\partial \mathrm{AR}}{\partial \Delta k} \right| = \frac{1 + \frac{\Delta k}{\sqrt{\Delta k^2 + k_c^2}}}{2k_c}. \tag{4}$$

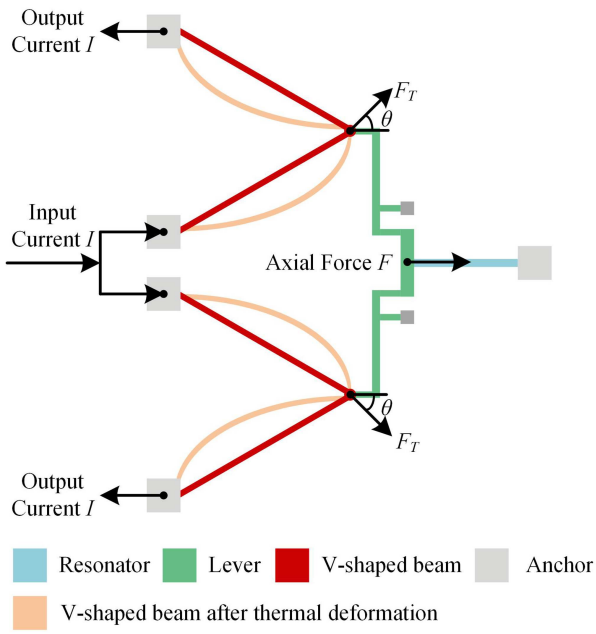

Figure 3 (Color online) Schematic diagram of the V-shaped beam.

The amplitude ratio output shows a nonlinear region when the disturbance is near zero; however, as the disturbance increases, the theoretical output sensitivity ($k_c \ll \Delta k$) gradually stabilizes, with the final output sensitivity approximated as follows:

$$S_k = \frac{1}{k_c}. \tag{5}$$

2.3 Theory analysis of the V-shaped beam

The analysis above demonstrates that WCRs operate as stiffness signal sensors, directly detecting changes in resonator stiffness. Thus, the core focus of this paper is to achieve high-sensitivity conversion of current signals into stiffness signals. This study employs a V-shaped beam structure for this conversion, with the structural schematic shown in Figure 3. Each resonator has two symmetric V-shaped beams positioned axially, with current applied to both beams simultaneously. Due to the symmetric structure, the current splits evenly between the two beams, causing them to expand thermally to the same extent. The heat transfer process for each V-shaped beam can be expressed as

$$\frac{I^2 \rho l_1}{A_1} = hA\Delta T, \tag{6}$$

where I is the current input into the V-shaped beam, ρ is the resistivity of the material, l_1 is the arm length of the V-shaped beam, h is the effective heat transfer coefficient to the external environment, A_1 is the effective cross-sectional area of the V-shaped beam, and A is the effective heat transfer area to the external environment.

From (6), it can be seen that when there is a temperature change ΔT, the free expansion of the V-shaped beam is

$$F_T = \alpha E \Delta T A_1, \tag{7}$$

where α is the coefficient of linear expansion of the material, E is the Young's modulus of the material.

The thermal expansion forces generated by the two V-shaped beams cancel each other in the direction perpendicular to the resonator, while stacking in the direction parallel to it. After amplification by the lever, the resulting axial force applied to the resonator is given by

$$F = 2DF_T \cos\theta = 2D\alpha E \Delta T A_1 \cos\theta, \tag{8}$$

where D is the amplification factor of the lever, θ is the angle between the thermal expansion force and the direction of the resonator.

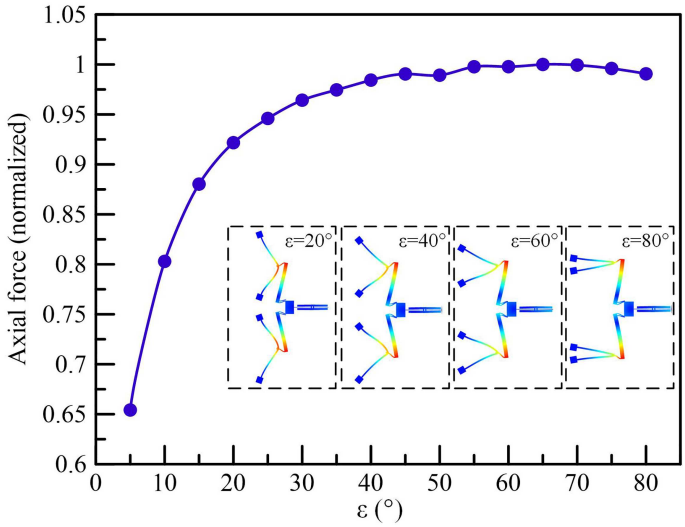

Figure 4 (Color online) The finite element simulation of V-shaped beam.

The analysis proceeds by beginning with the one-dimensional Euler-Bernoulli equation and following this by proceeding with the Rayleigh-Ritz energy method. The vibration of the resonator can be simplified as a doubly clamped beam under axial force where the stiffness change caused by axial force equals to [27]

$$\Delta k = \frac{4.85F}{L}, \tag{9}$$

where L is the length of the resonator.

According to (6), (8), and (9), the stiffness perturbation caused by thermal expansion force to the resonator can be written as

$$\Delta k = \frac{9.7I^2\rho l_1 D\alpha E\cos\theta}{hAL}. \tag{10}$$

According to (3) and (10), the amplitude ratio in the first mode can be obtained ($\Delta k \gg k_c$)

$$\mathrm{AR} \approx \mathrm{AR}_0 + \frac{\Delta k}{k_c} = \mathrm{AR}_0 + \frac{9.7I^2\rho l_1 D\alpha E\cos\theta}{k_c hAL}, \tag{11}$$

where AR_0 is the initial working point of the current sensor.

The linear output equation for the input current I obtained by squaring equation (11) is

$$\mathrm{AR}_{\mathrm{sq}} = \sqrt{\mathrm{AR} - \mathrm{AR}_0} = \sqrt{\frac{9.7\rho l_1 D\alpha E\cos\theta}{k_c hAL}}I. \tag{12}$$

2.4 Finite element simulation of the current sensor

Optimizing the structural parameters of the device is crucial for enhancing current sensing performance, with the V-shaped beam angle being particularly important due to its direct impact on thermal force transmission. To determine the optimal angle, finite element simulations were conducted to analyze the relationship between the direction of thermal expansion force and the resulting axial force applied to the resonator. ε is the angle between the V-shaped beam and the direction perpendicular to the resonator. As shown in Figure 4, the efficiency of axial force transmission gradually increases, reaching its maximum at almost 60°. When ε continues to increase, it can easily lead to unstable force transmission, manifesting as a decrease in transmission efficiency. Therefore, this study designed the angle of the V-shaped beam to be 60°.

To evaluate the potential impact of the auxiliary components on the dynamic response of the primary resonator, the mode simulations were conducted. As shown in Figure 5, the resonant of frequency of resonator, lever, and V-shaped beam are 22763.6, 65546.4, and 123337.6 Hz, respectively. The results show that the work resonant mode of the resonator appears at a much lower frequency compared to the lever and V-shaped beams. Therefore, the lever and V-shaped beams remain almost static during resonator operation. No abnormal vibrations or modal couplings were observed in the work frequency. These findings confirm that the auxiliary structures primarily serve

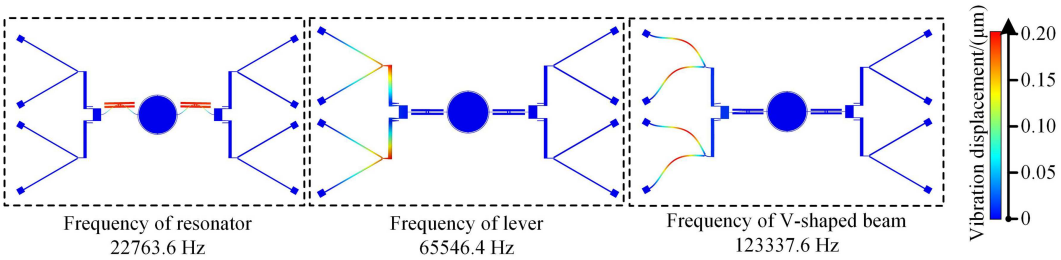

Figure 5 (Color online) The resonant frequency of the structure.

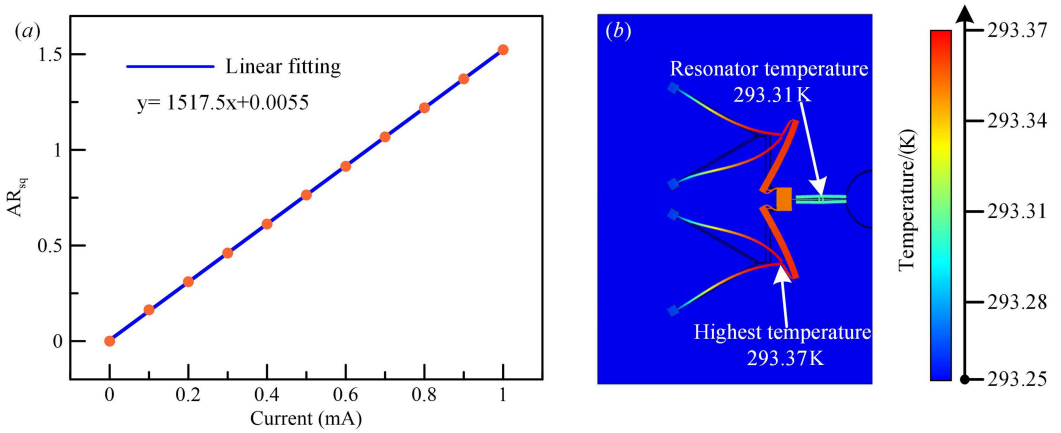

Figure 6 (Color online) (a) The finite element simulation of measuring range; (b) the finite element simulation of temperature variation.

as quasi-static force transmission elements and do not introduce unintended dynamic interference to the resonator's response.

When a current flows through the structure, it generates heat, leading to a temperature change on the surface of the resonators. Since the resonators are made of semiconductor silicon, this temperature variation alters the material properties, affecting the overall system dynamics. Finite element simulations are conducted to verify the temperature distribution on the resonator surface within a specific current range, ensuring the feasibility of this thermal effect in practical applications. The finite element simulation results are shown in Figure 6. As shown in Figure 6(a), within the input current range of 1 mA, the input current exhibits a linear relationship with the output AR_{sq}, validating the effectiveness of the proposed method. A temperature simulation was conducted with an initial setting of room temperature (293.15 K). As shown in Figure 6(b), under an input current of 1 mA, the maximum surface temperature of the device reached 293.37 K, while the resonator surface temperature stabilized at 293.31 K. This maximal temperature variation, approximately 0.05%, confirms that within the 1 mA measurement range, the effect of Joule heating on the system's performance is negligible.

3 Fabrication and experimental setup

3.1 Device fabrication

The current sensor was fabricated using a silicon-on-insulator (SOI) process [28, 29], as illustrated in Figure 7(a). The fabrication steps include: (1) depositing and patterning photoresist on the substrate; (2) performing ICP etching on the substrate trenches and removing the oxide layer; (3) depositing and patterning photoresist on the front side; (4) patterning metal electrodes; (5) defining the device structure and bonding it to a carrier wafer; and (6) using DRIE to etch the device layer, followed by the removal of photoresist and the carrier wafer. Finally, the devices were released in an HF solution. The device processing results are shown in Figure 7(b).

3.2 Experimental setup

The performance of the current sensor was evaluated in a vacuum chamber at a pressure of 0.022 Pa using both open-loop and closed-loop schemes. The schematic of the experiment measurement is depicted in Figure 8(a). Current

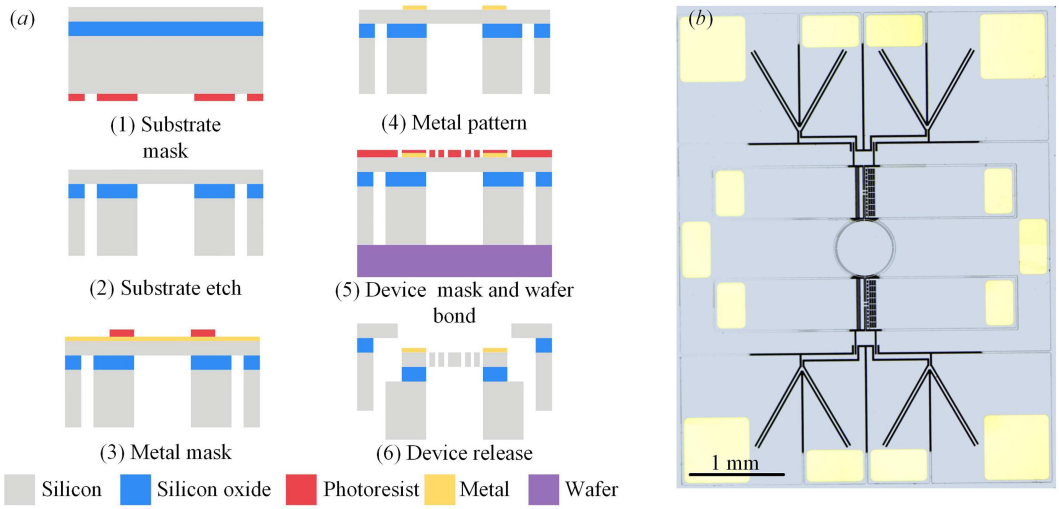

Figure 7 (Color online) (a) The current sensor process; (b) optical diagram of the current sensor.

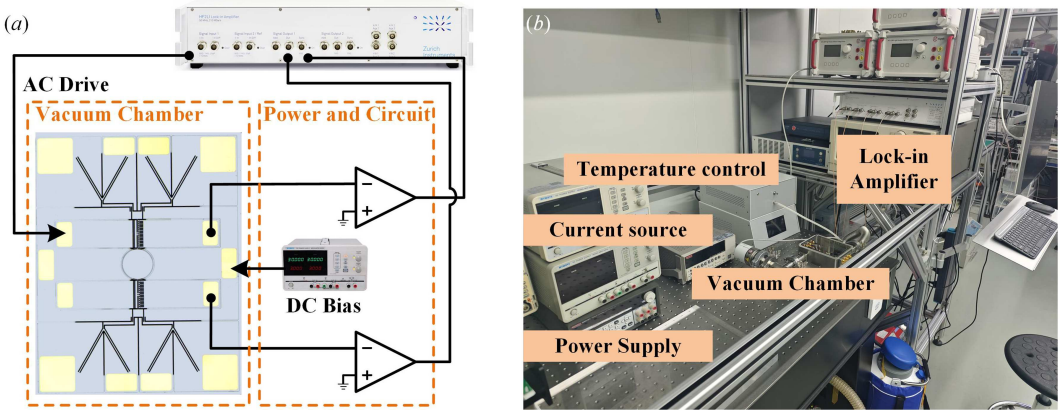

Figure 8 (Color online) (a) Schematic of the experiment measurement; (b) the photo of the experimental setup.

sensor is applied to a DC bias voltage of 10 V by DC power. The photo of the experiment setup is illustrated in Figure 8(b).

In the open-loop schematic, a sweep signal from a lock-in amplifier (Zurich Instruments HF2LI) is applied to the drive electrode. The amplitude signals from the resonators are first amplified by charge amplifiers and then measured by the lock-in amplifier to detect the mode localization phenomenon in the current sensor. In the closed-loop schematic, the resonator is also driven and detected by a lock-in amplifier. Additionally, the lock-in amplifier provides a PID controller and numerical oscillator to track and lock in the phases of the resonators, ensuring they vibrate in the desired working mode.

4 Results and discussion

4.1 Frequency responses

Under the open-loop control, the amplitude-frequency response and phase-frequency response of the current sensor were tested. As displayed in Figure 9(a), the available vibration modes of resonators 1 and 2 were 21756.3 and 21762.8 Hz, respectively, resulting in a frequency difference of 6.5 Hz. The -3 dB bandwidth of the resonator is 3.0 Hz, therefore the quality factor Q is approximately 7252. Based on the frequency difference and resonant frequency, the coupling coefficient κ of WCRs can be calculated to be $\kappa = 6.5/21756.3 \approx 3 \times 10^{-4}$. The smaller the coupling coefficient, the higher the sensitivity of the mode-localized sensor [30]. The κQ is about $2.2 > 1$, ensuring that WCRs work in the mode-localization regime without mode mixing [26].

As shown in Figure 9(b), in the first mode, the phase difference between resonators 1 and 2 is about 180°, whereas in the second mode, their phases are nearly identical. A 180° phase difference in the output signal corresponds to

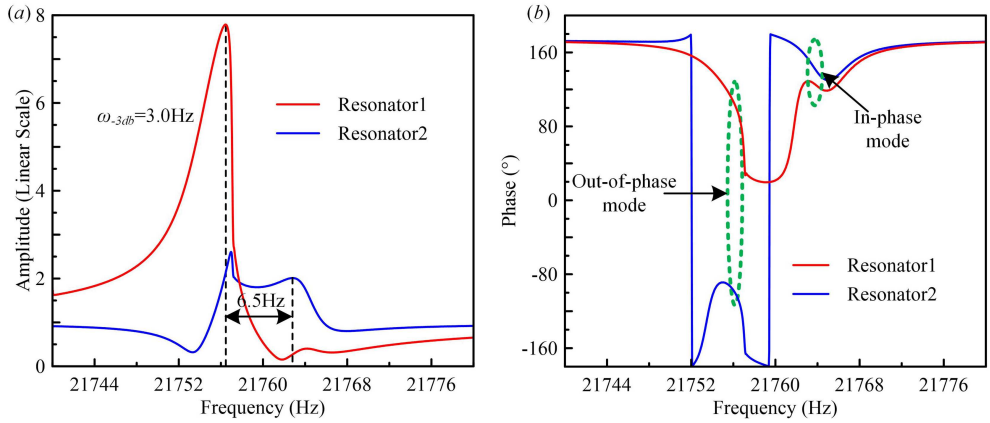

Figure 9 (Color online) (a) Amplitude-frequency of resonator 1 and resonator 2; (b) phase-frequency of resonator 1 and resonator 2.

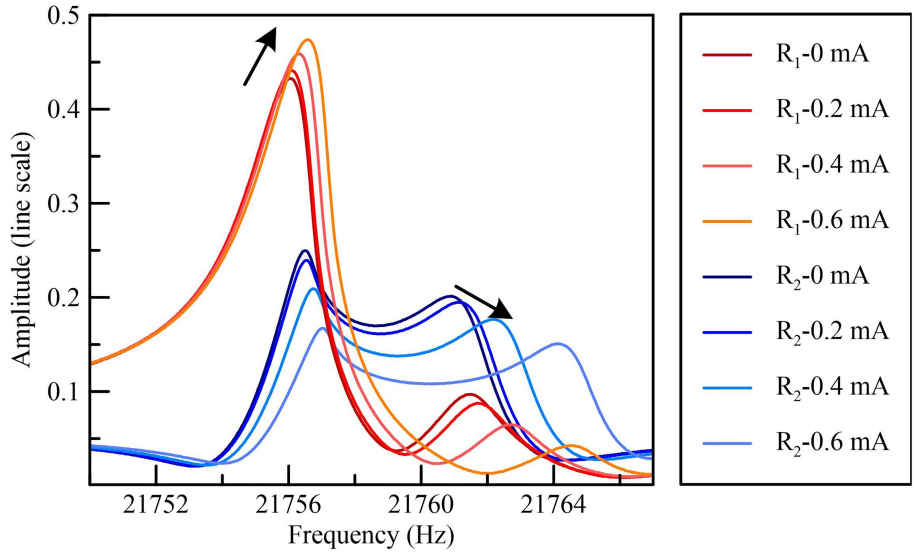

Figure 10 (Color online) Amplitude-frequency with different current.

an out-of-phase vibration mode of the sensor, while the same phase difference indicates an in-phase mode. This study chooses the first-order mode, which is the reverse mode, as the working mode.

4.2 Mode localization phenomenon

To observe the phenomenon of mode localization, the amplitude-frequency response of the current sensor with varying input currents was tested. As shown in Figure 10, only the peak value of the first mode of resonator 1 increased whereas the other three modes decreased. This result demonstrates that energy converges from resonator 2 into the 1st mode of resonator 1, which verifies that the mode-localized current sensor responds to current variations and observes the phenomenon of mode localization.

4.3 Sensitivity

To assess the sensor's sensitivity, a precision current source (Keithley 6220) was used to apply a standard current ranging from 0 to 1 mA with a step of 0.1 mA. The sensitivity measurements were conducted under closed-loop control to ensure accuracy. As shown in Figure 11, the AR increased from 1.67 to 5.03 with increasing current, exhibiting a quadratic relationship that aligns well with the theoretical model in (11). The maximum sensitivity reached 6053/A in 0.9–1 mA. The result is 10 times higher than in previous work [25], highlighting the sensor's potential for ultra-sensitive current detection.

To reduce nonlinearity, a dimensional transformation was applied to the output to establish a linear relationship between the input current and the output response. As shown in Figure 11, the transformed output, AR_{sq}, exhibits a near-linear correlation with the input current. The fitted linear equation is presented in (13), the sensitivity

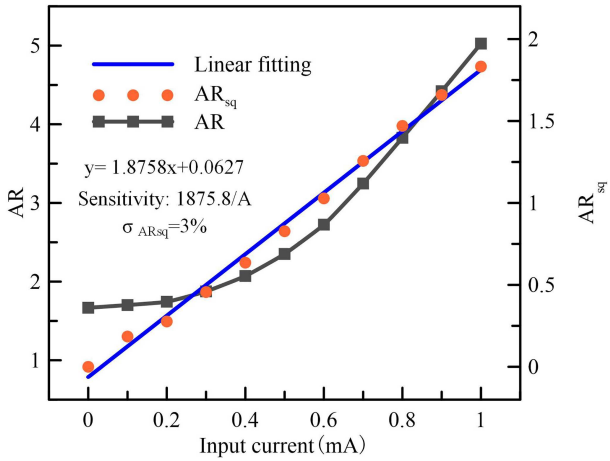

Figure 11 (Color online) AR and AR_{sq} versus input current.

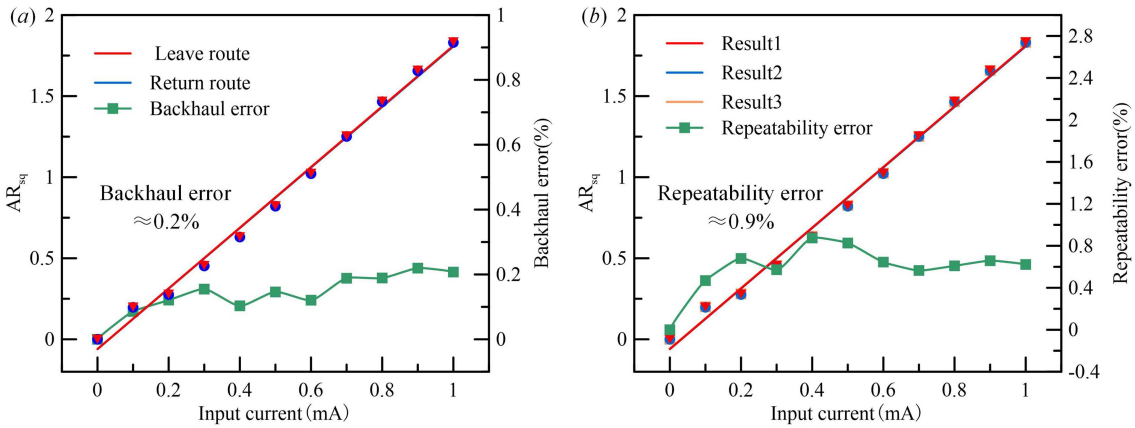

Figure 12 (Color online) (a) Backhaul errors of the current sensor; (b) repeatability errors of the current sensor.

was determined to be 1875.8/A, and the nonlinearity error was about 3%. This sensitivity result is slightly higher than the finite element simulation predictions, likely due to fabrication-induced variations. Specifically, processing imperfections may have resulted in a reduction in the coupling beam dimensions, thereby decreasing the coupling stiffness. As weaker coupling enhances sensitivity, this reduction in stiffness is the most probable cause of the observed deviation.

$$Y = 1.8758 \times X + 0.0627. \tag{13}$$

4.4 Backhaul and repeatability error

Maintaining low Backhaul and repeatability error is crucial to the accuracy measure current. For accurate evaluation of the performance of current sensors, these errors were carefully evaluated. To assess backhaul and repeatability, the current was measured many times independent. This test helps verify the stability of the current sensor.

As shown in Figure 12(a), the backhaul error is calculated as

$$\sigma_h = \frac{|h_{\max}|}{A} \approx 0.2\%, \tag{14}$$

where $h_{\max}$ is the largest difference between the curves of forward leave and return route.

As shown in Figure 12(b), the repeatability error is calculated as

$$\sigma_R = \frac{3\delta}{A} \approx 0.9\%, \tag{15}$$

where δ is the largest difference among the five curves for forward and reverse travel.

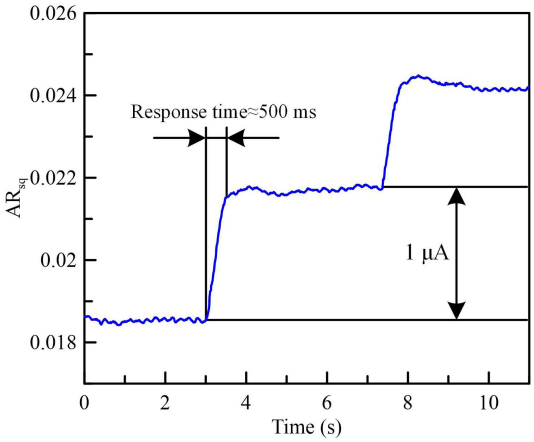

Figure 13 (Color online) Response time of the current sensor.

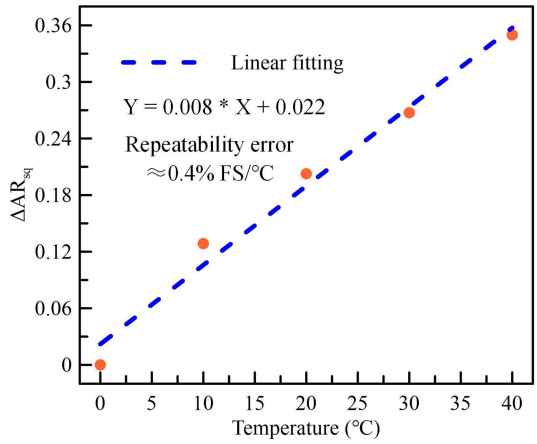

Figure 14 (Color online) Zero drift of the current sensor.

The sensor demonstrated exceptional stability, with a return error of just 0.2% and a repeatability error of 0.9%, ensuring highly reliable measurements. These results confirm the sensor's stability, further highlighting its potential for precise and consistent current detection.

4.5 Response time

A small current step test on the sensor was conducted to obtain its response time. Using a current source (Keithley 6220) input with a step of 1 μA, the test results are shown in Figure 13. The current sensor has an obvious step for a current of 1 μA, demonstrating its ability to detect small currents. The response time is about 500 ms.

4.6 Zero drift

Ambient temperature fluctuations can cause significant zero drift by inducing thermal deformation and stiffness changes in the V-shaped beams and coupled structures. Conducting zero drift experiments is crucial as it validates sensor stability. Experiments were conducted using temperature control equipment within the range of 0°C–40°C, with a step of 10°C. After the temperature stabilizes, collect 30 s of current sensor output as the zero point output at that temperature. The test results are shown in Figure 14. When the temperature rises from 0°C to 40°C, the zero drift increases from 0 to 0.35, with an average drift of 0.4%FS/°C.

4.7 Noise floor, resolution and dynamic range

The sensor was tested under closed-loop control using a lock-in amplifier, which simultaneously recorded the output signal of the current sensor. The data acquisition was performed at a sampling rate of 225 Hz over a continuous period of about one hour to ensure sufficient statistical accuracy. The collected signal was then processed and transformed into AR_{sq} for further analysis. To evaluate the sensor's noise characteristics, the noise spectral density of the signal was computed. As shown in Figure 15, the noise floor of AR_{sq} was $5 \times 10^{-6}/\sqrt{\mathrm{Hz}}$ at 1 Hz. The sensitivity of the current sensor, based on the AR_{sq}, was 1875.8/A. The noise floor of the current sensor could then be calculated as

$$I_{\mathrm{noise}} = \frac{5 \times 10^{-6}/\sqrt{\mathrm{Hz}}}{1875.8/\mathrm{A}} = 2.7\ \mathrm{nA}/\sqrt{\mathrm{Hz}}. \tag{16}$$

The -3 dB bandwidth $\omega_{-3\ \mathrm{dB}}$ of the current sensor is about 3.0 Hz and the noise equivalent bandwidth NEB is 1.57× larger than the $\omega_{-3\ \mathrm{dB}}$. The resolution of the current sensor can be calculated by [31]

$$\mathrm{Res} = I_{\mathrm{noise}} \times \sqrt{\mathrm{NEB}} = 5.9\ \mathrm{nA}. \tag{17}$$

The measurement range is 1 mA and the resolution is 5.9 nA. Therefore, the dynamic range of the current sensor is calculated as

$$\mathrm{DR} = 20 \times \lg\left(\frac{\mathrm{MR}}{\mathrm{Res}}\right) = 104.6\ \mathrm{dB}. \tag{18}$$

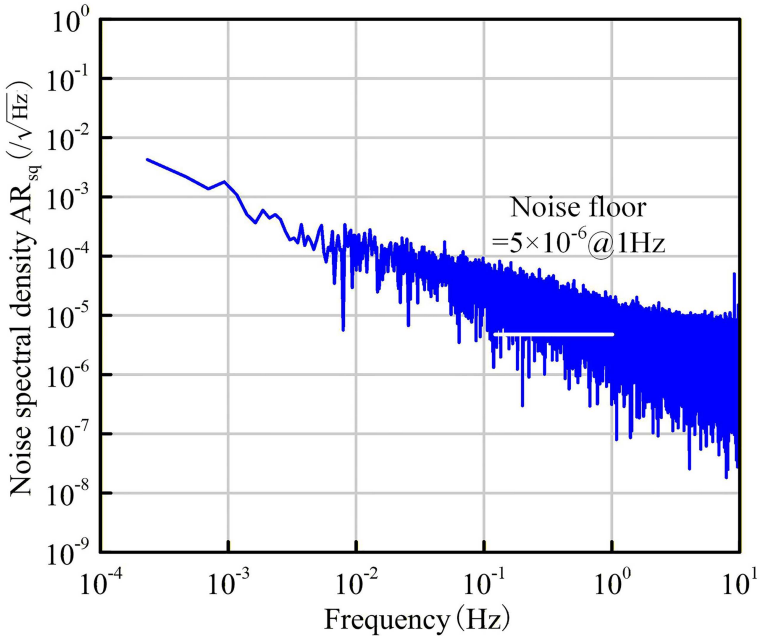

Figure 15 (Color online) Noise spectral density of the output.

4.8 Comparison of different current sensors

The performance comparison between the proposed sensor and other current sensors is summarized in Table 2. Compared to MEMS sensors based on magnetic metal film, giant magnetoresistance, and shunt resistor principles, the proposed current sensor achieves significantly higher sensitivity due to the combined effects of mode localization and heat-sensitive detection, thereby enhancing its detection limit. Furthermore, unlike magnetic principle-based sensors, it is entirely immune to external magnetic interference, overcoming a major limitation of such technologies.

Furthermore, the highest-resolution range of the Fluke 18B+ multimeter, which offers a lower measurement range than the current sensor, is selected for comparison. The current sensor achieves a resolution of 5.9 nA, substantially surpassing that of the Fluke 18B+. Moreover, it exhibits an exceptional dynamic range of 104.6 dB, demonstrating its strong potential for high-precision current sensing applications.

Table 2 Comparison of different current sensors.

Performance indexes	This work	Previous work [25]	Magnetic metal film [6]	Giant magnetoresistance [8]	Fluke 18B+
Sensitivity	AR: 6053/A; AR_{sq}: 1875.8/A	AR: 567/A	$5\sqrt{\text{Hz}}$/A	22 V/A	–
Resolution	5.9 nA	183.6 nA	–	Sub-mA	100 nA
Measurement range	1 mA	2 mA	1.5 A	2 mA	400 μA
Dynamic range	104.6 dB	80.7 dB	–	–	72 dB

5 Conclusion

In this study, an ultrasensitive MEMS current sensor based on mode localization and thermal sensitivity was proposed and experimentally validated. By leveraging the thermal expansion effect induced by current flow, the sensor achieves the ultrasensitive measurement of current. Experimental results demonstrated a maximum sensitivity enhancement of 10 times compared to previous mode-localized current sensors based on shunt resistors. By output linearization, the input-output relationship is transformed from a quadratic relationship to a linear one, with a return error of 0.2% and a repeatability error of 0.9%. The sensor achieved a noise floor of 2.7 nA/$\sqrt{\text{Hz}}$, resolution of 5.9 nA, and dynamic range of 104.6 dB, making it the highest-resolution MEMS current sensor reported to date.

The proposed sensor offers significant advantages, including immunity to external magnetic interference and excellent miniaturization potential, making it highly suitable for compact, high-resolution current sensing applications. Future work will focus on further improving linearity and optimizing structural design to enhance performance and expand its application range.

Acknowledgements This work was supported by National Natural Science Foundation of China (Grant Nos. 52435012, 52475606), National Key Research and Development Program of China (Grant Nos. 2024YFB4612800, 2023YFB3208800), and Innovation Capability Support Program of Shaanxi (Grant No. 2024RS-CXTD-7).

References

1 Bourkeb M, Ondel O, Scorretti R, et al. Improved AC current measurement approach in multiphase cable using proper orthogonal decomposition. European Phys J Appl Phys, 2013, 64: 24509
2 Ding L, Ma C, Li L, et al. A photoelectrochemical sensor for hydrogen sulfide in cancer cells based on the covalently and in situ grafting of CdS nanoparticles onto TiO_2 nanotubes. J Electroanal Chem, 2016, 783: 176–181
3 Zhou C-Y, Su H, Mao R-S, et al. An accurate low current measurement circuit for heavy iron beam current monitor. Nuclear Instrum Method Phys Res Section B, 2012, 280: 84–87
4 Popovic R S. Not-plate-like Hall magnetic sensors and their applications. Sens Actuat A-Phys, 2000, 85: 9–17
5 Watanabe Y, Kato M, Yahagi T, et al. MEMS Rogowski coil current sensor with spiral return coil. Electrical Eng Japan, 2022, 215: e23408
6 Phan T A, Hara M, Oguchi H, et al. Current sensors using Fe-B-Nd-Nb magnetic metallic glass micro-cantilevers. MicroElectron Eng, 2015, 135: 28–31
7 Shanglin Y, Rong F. Flexible-substrate fluxgate current sensor based on MEMS technology. Sens Mater, 2020, 32: 3083–3094
8 Garcia-Romeo D, Medrano N, Calvo B, et al. Sub-mA current measurement by means of GMR sensors and state of the art lock-in amplifiers. In: Proceedings of IEEE International Conference on Industrial Technology, Seville, 2015. 3377–3381
9 Yang Z, Wang Z, Liu M, et al. Non-contact current sensing system based on the giant magnetoimpedance effect of CoFeNiSiB amorphous ribbon meanders. Micromachines, 2024, 15: 161
10 Liu Q, Xie F, Peng X, et al. Millimeter-scale temperature self-calibrated diamond-based quantum sensor for high-precision current sensing. Adv Quantum Tech, 2023, 6: 2300210
11 Jiang R, Zheng Y. Fiber-optic current sensing based on reflective polarization-bias-added structure. IEEE Sens J, 2024, 24: 292–302
12 Sun H, Huang S, Peng L. High-current sensing technology for transparent power grids: a review. IEEE Open J Ind Electron Soc, 2024, 5: 326–358
13 Ajayan A, Rajan L, Prakash S, et al. Macromolecular sensing motors from conducting polymers: polyaniline/methylcellulose composites as stable current sensing supercapacitors. Int J Biol Macromol, 2024, 279: 135312
14 Tao K, Tang L, Wu J, et al. Investigation of multimodal electret-based MEMS energy harvester with impact-induced nonlinearity. J Microelectromech Syst, 2018, 27: 276–288
15 Seshia A A, Palaniapan M, Roessig T A, et al. A vacuum packaged surface micromachined resonant accelerometer. J Microelectromech Syst, 2002, 11: 784–793
16 Chorsi M T, Curry E J, Chorsi H T, et al. Piezoelectric biomaterials for sensors and actuators. Adv Mater, 2019, 31: 1802084
17 Teng G, Yang C H, Quan A J, et al. Extracting mechanical quality factor and eliminating feedthrough using harmonics of thermal-piezoresistive micromechanical resonators. Microsystem Nanoeng, 2025, 11: 30
18 Spletzer M, Raman A, Wu A Q, et al. Ultrasensitive mass sensing using mode localization in coupled microcantilevers. Appl Phys Lett, 2006, 88: 254102
19 Zhang H, Sobreviela G, Chen D, et al. A high-performance mode-localized accelerometer employing a quasi-rigid coupler. IEEE Electron Device Lett, 2020, 41: 1560–1563
20 Kang H, Ruan B, Hao Y C, et al. Mode-localized accelerometer with ultrahigh sensitivity. Sci China Inf Sci, 2022, 65: 142402
21 Yan Z M, Hao Y C, Li W M, et al. A mode-localized Lorentz force magnetometer with 1.6 $\mu T/\sqrt{Hz}$ resolution. In: Proceedings of the 20th International Conference on Solid-State Sensors, Actuators and Microsystems and Eurosensors XXXIII (Transducers and Eurosensors), Berlin, 2019. 1815–1818
22 Thiruvenkatanathan P, Yan J, Seshia A A, et al. Ultrasensitive mode-localized micromechanical electrometer. In: Proceedings of IEEE International Frequency Control Symposium, Newport Beach, 2010. 91–96
23 Hao Y, Liang J, Kang H, et al. A micromechanical mode-localized voltmeter. IEEE Sens J, 2021, 21: 4325–4332
24 Zhang H, Li H, Sun J, et al. Coherent energy transfer in coupled nonlinear microelectromechanical resonators. Nat Commun, 2025, 16: 3864
25 Li H, Zhang Z, Zu L, et al. Micromechanical mode-localized electric current sensor. Microsystem Nanoeng, 2022, 8: 42
26 Zhang H, Li B, Yuan W, et al. An acceleration sensing method based on the mode localization of weakly coupled resonators. J Microelectromech Syst, 2016, 25: 286–296
27 Lee J, Rhim J. Temperature compensation method for the resonant frequency of a differential vibrating accelerometer using electrostatic stiffness control. J Micromech Microeng, 2012, 22: 095016
28 Hao Y, Xie J, Yuan W, et al. Dicing-free SOI process based on wet release technology. Micro Nano Lett, 2016, 11: 775–778
29 Hao Y, Wang Y, Liu Y, et al. An SOI-based post-fabrication process for compliant MEMS devices. J Micromech Microeng, 2024, 34: 045005
30 Thiruvenkatanathan P, Yan J, Seshia A A. Differential amplification of structural perturbations in weakly coupled MEMS resonators. IEEE Trans Ultrason Ferroelect Freq Contr, 2010, 57: 690–697
31 Instruments T. Noise Analysis in Operational Amplifier Circuits. Application Report, SLVA043B, 2007